

Ultrafast processes in graphene: from fundamental manybody interactions to device applications

Winnerl, S.; Mittendorff, M.; König-Otto, J. C.; Schneider, H.; Helm, M.; Winzer, T.; Knorr, A.; Malic, E.;

Originally published:

August 2017

Annalen der Physik 529(2017)11, 1700022

DOI: <https://doi.org/10.1002/andp.201700022>

Perma-Link to Publication Repository of HZDR:

<https://www.hzdr.de/publications/Publ-24859>

Release of the secondary publication
on the basis of the German Copyright Law § 38 Section 4.

Article type: Feature article

Ultrafast processes in graphene: from fundamental manybody interactions to device applications

Stephan Winnerl^{1,}, Martin Mittendorff^{2,1}, Jacob C. König-Otto^{1,3}, Harald Schneider¹, Manfred Helm^{1,3}, Torben Winzer⁴, Andreas Knorr⁴, and Ermin Malic⁵*

*Corresponding Author: E-mail: s.winnerl@hzdr.de

¹Helmholtz-Zentrum Dresden-Rossendorf, P.O. Box 510119, 01314 Dresden, Germany

²University of Maryland, College Park, Maryland 20742, USA

³Technische Universität Dresden, 01062 Dresden, Germany

⁴Technische Universität Berlin, Hardenbergstraße 36, 10623 Berlin, Germany

⁵Chalmers University of Technology, SE-41296 Göteborg, Sweden

A joint experiment-theory investigation of the carrier dynamics in graphene, in particular in the energetic vicinity of the Dirac point, is reviewed. Radiation of low photon energy is employed in order to match the intrinsic energy scales of the material, i.e. the optical phonon energy (~ 200 meV) and the Fermi energy (10-20 meV), respectively. Significant slower carrier cooling is predicted and observed for photon energies below the optical phonon energy. Furthermore, a strongly anisotropic distribution of electrons in k -space upon excitation with linearly polarized radiation is discussed. Depending on photon energy, the anisotropic distribution decays either rapidly via optical phonon emission, or slowly via non-collinear Coulomb scattering. Finally, a room temperature operated ultra-broadband hot-electron bolometer is demonstrated. It covers the spectral range from the THz to visible region with a single detector element featuring a response time of 40 ps.

1. Introduction

Graphene, a single layer of sp^2 hybridized carbon atoms arranged in a hexagonal lattice, is the firstly discovered material of a new class of atomically thin two-dimensional crystals [1,2]. It features a gapless band structure in which valence and conduction bands touch each other at the corners of the hexagonal Brillouin zone, namely in the K and K' Dirac points. This band structure has already been calculated in 1947 as a model system for the tight-binding approach [3]. In the vicinity of these Dirac points, there is perfect electron hole symmetry. The word “Dirac point” highlights the similarities between graphene electrons and massless relativistic particles described by the Dirac equation [4]. The similarity comprises the linear relationship between energy and momentum and a quantum number named pseudospin, which is related to the fact that the primitive graphene lattice contains two carbon atoms. In electrical transport, this band structure results in a peculiarity named Klein tunneling [5]. As a practical example, Klein tunneling implies that charge carriers move across a pn-junction in graphene at 100 % transmission rate when approach the junction at normal incidence [6]. The most prominent optical property of graphene is the so-called universal absorption [7]. It means that the interband absorption is independent of the photon energy in the linear range where the band structure can be described by Dirac cones. Moreover, the absorption is also independent of material parameters and just determined by natural constants. A single layer of graphene absorbs $\pi\alpha \approx 2.3$ % of the incident radiation, where $\alpha \approx 1/137$ is the fine-structure constant. For higher photon energies, the absorption increases and reaches a maximum at the van Hove singularity corresponding to absorption at the saddle point (M point) of the Brillouin one. In this region, corresponding to photon energies of 4 – 5 eV, excitonic renormalization is important, while in the vicinity of the Dirac point excitonic effects are negligible [8]. In the vicinity of the Dirac points, the pseudospin of

Dirac fermions in graphene manifests itself in a selection rule for excitation, which will be discussed in detail in this article.

Graphene fabrication techniques as well as electronic, photonic and bio-applications are reviewed in Ref. [9]. Basic static optical properties and photonic device applications are discussed in Ref. [10], the science and technology roadmap for graphene evaluated by the European Flagship is presented in Ref. [11]. Furthermore there is an extensive review article on photodetectors based on graphene and other two-dimensional materials [12]. In this feature article we focus on the ultrafast optical properties in graphene.

The understanding of the carrier dynamics in a fairly novel material like graphene is of strong fundamental interest. Furthermore, the knowledge of the carrier dynamics is of key importance for the development of fast electronic and photonic devices [10,11]. A number of degenerate [13,14,15,16] and two-color pump-probe [17,18,19,20,21] studies, involving pump photon energies in the eV range, have identified thermalization on a sub-100 fs timescale and carrier cooling on a timescale of 100 fs to a few ps as the main processes involved in the relaxation. More recently, these studies were complemented by time- and angle-resolved photoemission spectroscopy (tr-ARPES), which allows one to fully trace the carrier occupation in energy and momentum space [22,23,24]. Particularly interesting findings related to the carrier dynamics are the observation of transient gain [25,26,27] and carrier multiplication [28,29,30,31,32,33,34,35,36]. The first effect is enabled by a bottleneck in the relaxation mainly due to the decrease of the density of states, the latter is mediated by efficient impact excitation of valence band electrons into the conduction band due to the vanishing band gap.

The joint experimental and theoretical study reviewed in this article is focused on the carrier dynamics at low photon energies with the main goal to disentangle the role of Coulomb and phonon related effects. This is typically difficult to achieve at high photon

energies as in this case, the two scattering mechanisms occur on similar time scales. Applying photon energies below the optical phonon energies, however, allows one to strongly suppress electron cooling via optical phonon emission (Section 2). Varying the photon energy around twice the value of the Fermi energy reveals the role of *interband* versus *intraband* absorption due to Pauli blocking effects. Furthermore, we investigate an unusual effect, namely a strongly anisotropic occupation of photoexcited carriers in k -space upon excitation with linearly polarized radiation (Section 3). We make use of this anisotropy to reveal an unusual graphene-specific behavior of Coulomb scattering, namely very fast collinear scattering accompanied by comparably slow non-collinear scattering. As an application, a graphene-based high-speed ultra-broadband detector operating in the spectral range from THz to visible (VIS) is demonstrated (Section 4). We note that our joint theory-experiment study of the carrier dynamics in Landau quantized graphene is reviewed in a separate article published in this special issue [E. Malic et al., citation when available].

2. The carrier-dynamics in the vicinity of the Dirac point

We have carried out degenerate and two-color pump-probe experiments in a wide range of photon energies (10 meV – 1.55 eV). To this end, various short-pulse laser systems, namely titanium-sapphire lasers, an optic-parametric oscillator and the free-electron laser FELBE were employed. The investigated graphene samples were produced by thermal decomposition of hexagonal SiC [37]. They consist of 30 to 50 electronically decoupled layers, grown on the C-terminated side of SiC [38]. While the layers close to the interface are highly doped, the majority of layers are almost intrinsic featuring Fermi energies in the range from 10 – 20 meV. In accord with earlier studies by Sun et al. [17,19] our experiments in the near-infrared (NIR) spectral range reveal a contribution from the highly doped layers, namely when the photon energy is in the vicinity of twice the Fermi energy of a particular doped layer

[39]. For all other photon energies, however, the response observed in the pump-probe experiments stems predominantly from the large number of almost intrinsic layers.

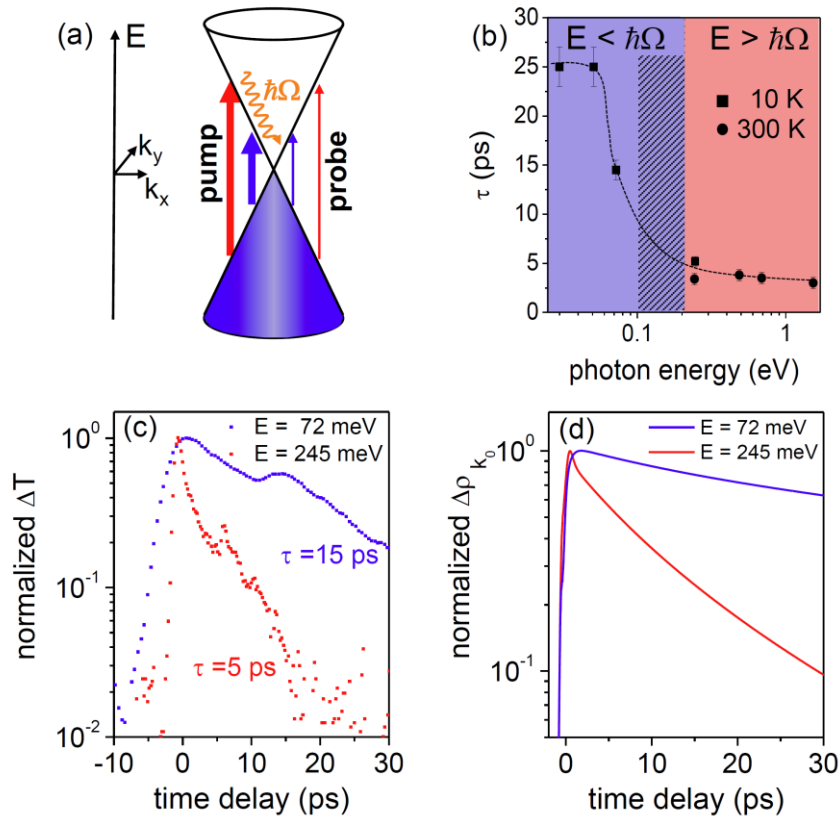


Figure 1: Principle of degenerate pump-probe spectroscopy at energies above (red arrows) and below (blue arrows) the optical phonon energy (a). Carrier cooling time τ deduced from degenerate pump-probe experiments at different photon energies (b). Different lattice temperatures are indicated by the type of symbol (circle or square). The dashed line is a guide for the eye; the shaded region indicates the region where the SiC substrate is opaque due to phonon absorption. Experimental transient induced transmission (c) and calculated change in occupation $\Delta\rho$ (d) of the occupation of the conduction band states corresponding to the optically addressed momentum k_0 . The figure is adapted from Ref. [39].

In **Figure 1** the results of degenerate pump-probe studies are summarized. The optical pumping results in an increased transmission due to Pauli blocking. The response in the NIR and mid-infrared (MIR) spectral range can be described by a double exponential decay with a fast component on the 100 fs timescale and a slower one in the range of a few ps. The first one is associated mainly with the thermalization of the initial non-equilibrium carrier distribution while the latter one is mainly connected to carrier cooling [40]. For low photon energies the decay is well described by a single exponential decay corresponding to carrier cooling. The dependence of the cooling time constant τ on photon energy is depicted in Figure 1b. A pronounced increase in the cooling time is observed as the photon energy is decreased to values below the optical phonon energy $\hbar\Omega \approx 200$ meV (Figure 1b and 1c). This directly shows that optical phonons constitute an efficient channel of carrier cooling and that this channel is strongly quenched at energies below $\hbar\Omega$ [40].

The performed experiments are complemented with microscopic theory that is based on graphene Bloch equations [41, 42] offering access to time-, momentum-, and angle-resolved carrier and phonon dynamics in optically excited graphene. Exploiting the Heisenberg equation of motion, we derive a set of coupled differential equations for the (i) microscopic polarization $p_{\mathbf{k}} = \langle a_{v\mathbf{k}}^+ a_{c\mathbf{k}} \rangle$ describing the optical excitation, (ii) carrier occupation probability $\rho_{\mathbf{k}} = \langle a_{\lambda\mathbf{k}}^+ a_{\lambda\mathbf{k}} \rangle$ in the state \mathbf{k} and the band λ , and (iii) phonon number $n_{\mathbf{q}}^j = \langle b_{j\mathbf{q}}^+ b_{j\mathbf{q}} \rangle$ in the mode j and with the momentum \mathbf{q} . We use the formalism of second quantization introducing creation and annihilation operators for electrons $(a_{\lambda\mathbf{k}}^+, a_{\lambda\mathbf{k}})$ and phonons $(b_{j\mathbf{q}}^+, b_{j\mathbf{q}})$. The equations explicitly include the carrier-light interaction as well as carrier-carrier and carrier-phonon coupling accounting for Coulomb- and phonon-induced intra- and interband scattering processes, respectively. The corresponding matrix elements are calculated with tight-binding wave functions in the nearest-neighbor approximation [41]. The many-particle

interactions are treated on the same microscopic footing within the second-order Born-Markov approximation [41,42]. For more details on the applied theoretical approach, see the related feature article Malic et al.

For comparison with the experiment the change in occupation $\Delta\rho$ of the optically probed states with momentum k_0 (i.e. $5.4 \times 10^7 \text{ m}^{-1}$ for $E = 72 \text{ meV}$ and $1.9 \times 10^7 \text{ m}^{-1}$ for $E = 245 \text{ meV}$, respectively) is calculated. This quantity is proportional to the change in transmission [43]. The calculated curves are in good qualitative and quantitative agreement with the experimental data (Figure 1c and 1d). The microscopic modelling also provides further insights that cannot be directly deduced from the experimental results. In particular, theory shows that even for photon energies below the optical phonon energy the cooling of the carrier distribution is still mainly caused by the emission of optical phonons. This is possible for hot carriers that are Coulomb scattered to states lying energetically above the initially optically populated states. Scattering via acoustic phonons, on the other hand, is much slower, namely on timescales of 100 ps [39,40]. Note that the dependence of τ on photon energy depicted in Figure 1b indicates that manybody Coulomb scattering is essential to understand the full cooling dynamics. In the absence of Coulomb scattering one would expect a sharp change in τ to appear at around $E = 2 \hbar\Omega \approx 400 \text{ meV}$, as this is the energy where optically excited carriers can scatter towards the bottom of the conduction band via optical phonon emission. However, around this energy the cooling time is rather constant. Consequently, the assumption of a distribution broadened by Coulomb scattering is essential to understand the observed trend. In two-color pump-probe experiments with blue-shifted probe beam we have obtained direct evidence for hot carriers above the optically excited states [39]. These results are in accord with the findings of other groups [16,21,44,45] that provide evidence for a fast thermalization on a sub-100 fs timescale. In Section 3 of this

article we discuss important aspects of Coulomb scattering, which is the main mechanism for thermalization.

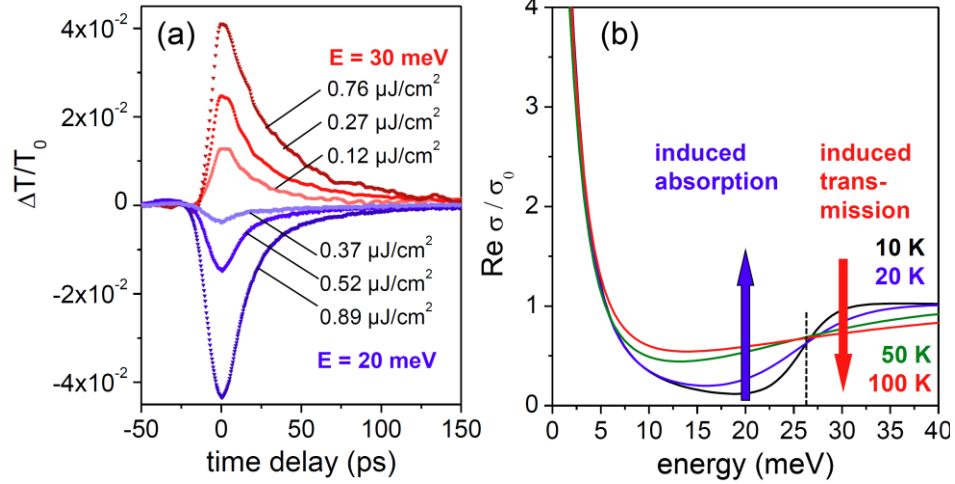


Figure 2: Relative pump induced transmission change for different pump fluences observed in degenerate pump-probe experiments at photon energies 20 meV and 30 meV, respectively (a). Calculated real part of the dynamic conductivity for different electron temperatures. The values are normalized to $\sigma_0 = e^2/4\hbar$, the universal conductivity value of graphene. The content of the Figure is published in Ref. [40].

At low photon energies a change in sign of the signal is observed in degenerate pump-probe experiments (**Figure 2a**). Positive signals, i.e. induced transmission, at higher photon energies correspond to a bleaching of the *interband* transition by Pauli blocking. For photon energies below $2E_f$, on the other hand, absorption increases with increasing electron temperature (Figure 2b), resulting in pump induced absorption [40]. For our samples this occurs in the spectral range where the *intra*band Drude peak at low energies merges with the broadened Fermi edge (Figure 2b). At low pump photon energies the change in sign is seen clearly in the experiments when the photon energy is tuned around $2E_f$. At higher fluences, however, the induced transmission can turn negative, even though $E > 2E_f$ (not shown). A

detailed analysis of experimental data in both transmission and reflection geometry has revealed that this change in sign is caused by pump-induced reflection [46]. The pump induced change in absorption is always negative, corresponding to bleaching of the transition. Nevertheless, the induced transmission turns negative as induced reflection over-compensates the reduced absorption at higher fluences [46]. Even though the bleaching of the interband transition most commonly dominates the response in the regime $E > |2E_f|$, there can be subtle effects of intraband absorption even at high energies. In particular, our microscopic modelling has revealed that pump-probe signals in the NIR range (i.e. $E \gg 2E_f$) can feature a small negative tail (induced absorption) after a much stronger positive peak (induced transmission) due to intraband absorption by the photoexcited carriers [47]. We have observed such signals experimentally [39, **Fehler! Textmarke nicht definiert.**], similarly to many other groups [16,18,48,49,50]. Before clarification by microscopic modelling, the origin of the small negative tails was controversially discussed. In particular, band renormalization effects [16], charge transfer from the substrate [18] and intraband absorption [50] have been suggested as possible mechanisms.

In the following we put the results presented in Figure 2 in a broader context and discuss a number of optical-pump THz-probe and nonlinear THz transmission experiments of other groups on different types of graphene samples. Note that the probe energy is the essential quantity here, since in many experiments the pump beam will result in a hot Fermi-Dirac distribution on timescales faster than the temporal resolution of the experiments. However, this argument may not always hold, as will be shown in section 3. In order to obtain a clear sign change when the photon energy is swept through $|2E_f|$, a number of requirements have to be fulfilled. As one can see from Figure 2b the sign change is expected if the region around the Fermi edge is clearly separated from the Drude peak. Another – less obvious – requirement is that the Fermi energy itself and the electron temperature are not too high. For

low Fermi energies and low electron temperatures the temperature dependence of the Fermi edge (more precisely: of the chemical potential) has only marginal influence on the dynamic conductivity (cf. Figure 2b). In the opposite case, a pronounced shift of the chemical potential and an according change of the Drude peak as a consequence of sum rule requirements are expected. This effect is discussed in more detail in section 4 (discussion of Figure 9). For the epitaxial graphene samples with a low Fermi energy for a large number of layers [51], an induced absorption is also seen in optical-pump THz-probe experiments using single cycle pulses. These THz pulses contain mostly photons of energies below 5 meV and therefore probe the Drude peak. This has been reported by the group of F. Rana [52,53] and we have obtained similar results for our samples [54]. Tuning the Fermi energy in gated single layer graphene also revealed induced absorption of THz photons of few meV for the case of almost neutral graphene [55,56]. At higher Fermi energies, the response switches to induced transmission. This has been explained as a switching from a semiconducting behavior for almost neutral graphene to metallic behavior for highly doped graphene. In the case of the metallic response the number of optically generated carriers is negligible compared to the carrier concentration due to doping. The material becomes more transparent since the Drude weight is reduced due to the temperature dependence of the chemical potential (see also section 4). In detail, also the dependence of the momentum relaxation time on electron temperature plays a role [44]. For graphene grown by chemical vapor deposition, featuring a high Fermi energy of about -300 meV, induced transmission was found [44,57,58] in accord with the studies on gated graphene. Note that single layer graphene samples, no matter if it is graphene grown by chemical vapor deposition, exfoliated and transferred to another substrate or grown epitaxially on the Si-terminated face of SiC, are highly doped. In contrast, the majority of layers in multilayer graphene on the C-terminated side of SiC is almost neutral. In summary, the response at low photon energies can be complex, depending mainly on the

Fermi energy of the sample, but also on the predominant scattering mechanism, the range of probed electron temperature and the exact photon energy of the probing radiation. Nevertheless the multitude of phenomena can be understood when the relevant dependencies are considered in the expression for the dynamic conductivity.

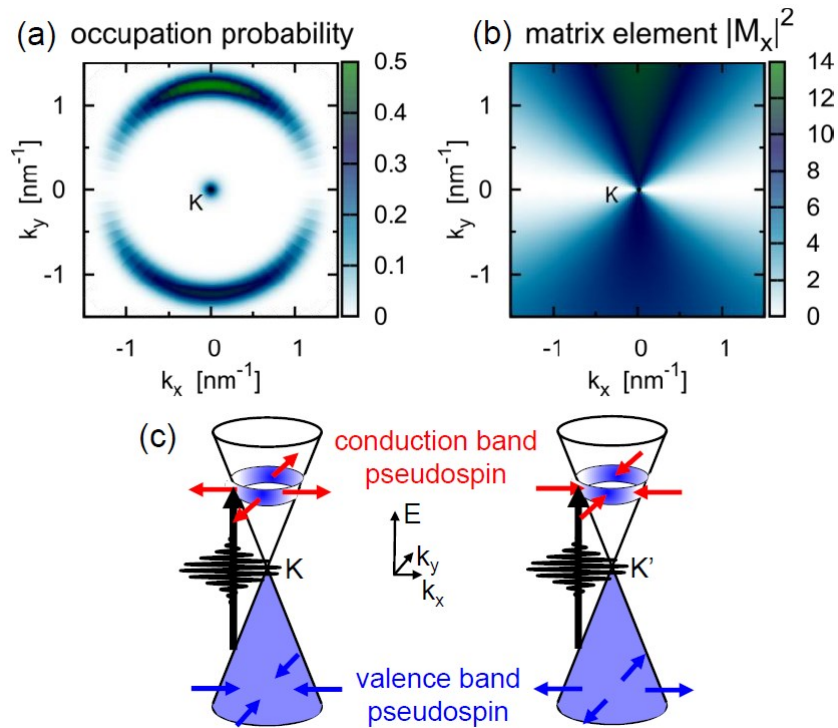


Figure 3: Calculated carrier occupation in the conduction band after excitation with a linearly polarized radiation pulse of $E = 1.55$ eV (a). The polarization of the radiation is along the x -direction. Squared matrix element for interband absorption for radiation polarized along the x -direction (b). Schematic representation of an optically induced anisotropic population in the conduction band and orientation of valence (blue) and conduction band (red) pseudospins in the Dirac cones at the K and K' points, respectively (c). Parts (a) and (b) are adapted from Ref. [42].

3. Optically induced anisotropy and its decay

Before discussing the role of Coulomb scattering versus phonon scattering, it is instructive to review specifics of interband excitation in graphene. The band structure of graphene is isotropic in the region described by Dirac cones. Consequently, the linear optical properties are isotropic, i.e. linear absorption does not depend on the orientation of the polarization of light with respect to the orientation of the crystal lattice. However, the preferential direction induced by the electric field of the radiation results in a two-fold symmetry of the squared interband transition matrix element that is calculated from the graphene tight binding wave functions (**Figure 3b**) [41,42,59]. Consequently, the conduction band occupation by carriers induced by linearly polarized radiation is strongly anisotropic (Figure 3a). In particular, electrons occupy preferentially states in the direction perpendicular to the direction of the electric field of the radiation (Figure 3a). Such an optically induced anisotropy was predicted by Grüneis et al. for graphite in the year 2003 [60]. In that article the anisotropy is directly linked to the lack of a leading-order quadratic term in the band structure. In materials with parabolic band structure and a typically complex structure of the valence band, effects related to spin-orbit coupling and selection rules with respect to circularly polarized radiation have been reported [61,62,63,64]. However, to our knowledge no anisotropy in the carrier occupation upon excitation with linearly polarized radiation has been observed in materials with parabolic dispersion in pump-probe experiments.

Finally, we note that the graphene Dirac equation, which describes the behavior of the carriers in the vicinity of the K and K' points of graphene, provide an elegant explanation of the optically induced anisotropy [65,66]. Dirac electrons in graphene feature a good quantum number called pseudospin, which is related to the graphene lattice containing two indistinguishable atoms per primitive unit cell [67,68]. The pseudospin is oriented parallel or antiparallel relative to \mathbf{k} for electrons and holes in the vicinity of the K and K' point,

respectively, as depicted in Figure 3c. The commutator relationship of the Hamiltonian for interband excitation with the pseudospin operator is zero along the momentum direction parallel to the electric field of the radiation. This means that the pseudospin is preserved. However, an interband excitation always requires a pseudospin flip (see Figure 3c). Therefore, a population of states with k -values in the direction of the electric field is inhibited [65,66].

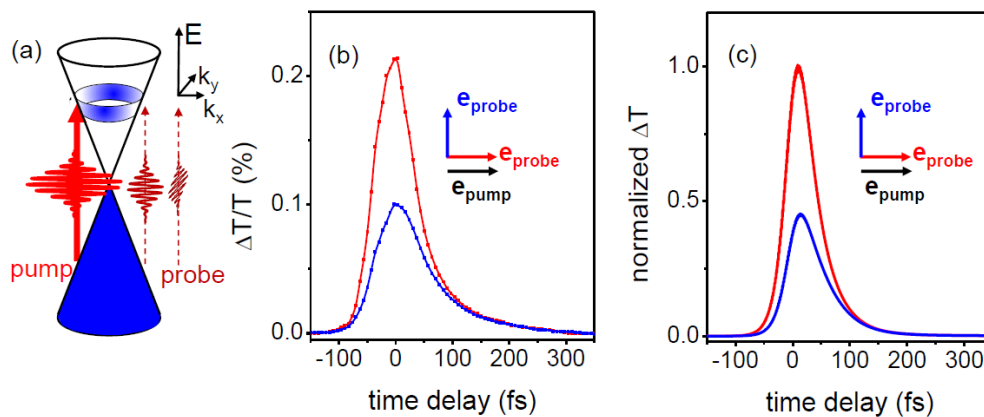


Figure 4: Scheme of degenerate pump-probe experiments with a probe beam polarization parallel or perpendicular to the pump beam orientation (a). Measured relative pump induced transmission change for the two polarization configurations (b). Calculated normalized transmission change for the two polarization configurations (c). Reprinted with permission from Ref. [72]. Copyright 2015 American Chemical Society.

First experimental evidence for an optically induced anisotropic carrier distribution was found in coherent [69,70] and incoherent [71] photocurrent measurements. In the following, we present direct evidence for the anisotropic carrier distribution in degenerate NIR pump-probe experiments at room temperature. To this end, both pump and probe beams are linearly polarized. The relative orientation of the probe beam is either parallel or perpendicular to the polarization of the pump beam (**Figure 4a**). Thus, we preferentially probe the states that are either strongly or weakly populated by the optical excitation, respectively (cf. Figure 3 and 4).

Note that this anisotropic excitation occurs simultaneously in both the K and K' Dirac cone. The observed induced transmission is more than twice as large for the parallel polarization configuration as compared to the perpendicular polarization scheme (Figure 4b) [72,73]. The anisotropic carrier distribution has also been observed in pump-probe experiments in reflection geometry [74,75]. Again, our experimental findings are in very good agreement with the predictions by microscopic theory (cp. Figure 4b and 4c) [72]. In particular, in both experiment and theory the transmission for both polarization directions equalizes within 150 fs after the excitation. Hence, an isotropic distribution is reached on this timescale. The microscopic theory shows that emission of optical phonons is responsible for rapidly reaching an isotropic distribution within this short time scale (**Figure 5**) [76]. In detail, mainly the Γ LO phonons (and to a much lesser extent the Γ TO phonons) result in the rapid formation of an isotropic contribution [76]. Furthermore, optical K phonons leading to intervalley scattering [77], contribute to the rapid formation of an isotropic carrier distribution in each Dirac cone [76].

Coulomb scattering, on the other hand, is preferentially collinear and therefore redistributes carriers rapidly along a given k -space orientation, but does not significantly redistribute carriers into states of different angles. This is a direct consequence of the angular dependence of intraband Coulomb scattering described by $|V|^2 \sim (1 + \cos \varphi_1)(1 + \cos \varphi_2)$, where V is the intraband Coulomb matrix element and φ_i is the angle between the momenta of initial and final state of two scattering electrons $i = 1, 2$ [76].

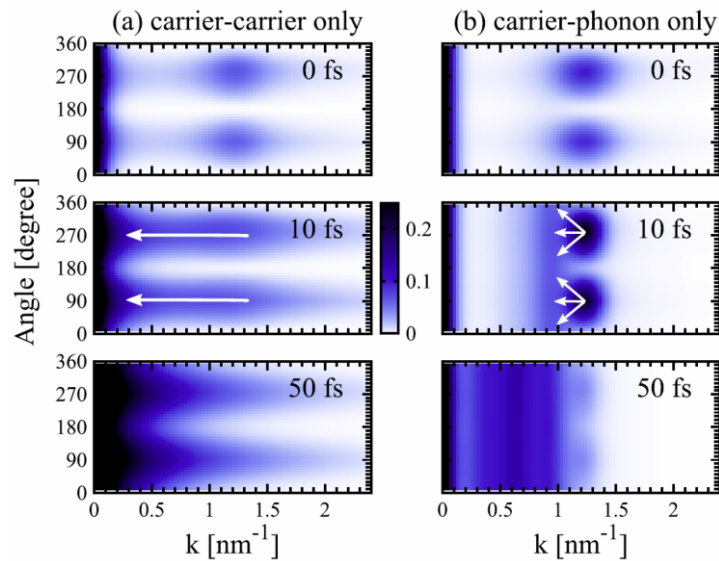


Figure 5: Angular distribution of the conduction band occupation upon excitation with linearly polarized light at an energy of 1.55 eV (polarization oriented at 0°). Figure reprinted from Ref. [76].

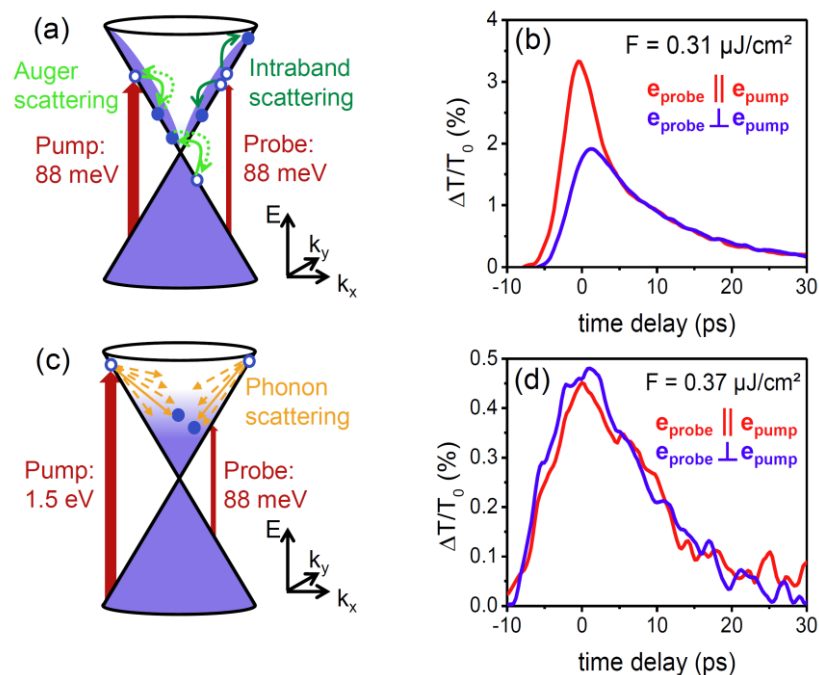


Figure 6: Principle of a single-color pump-probe experiment (a) and corresponding experimental induced transmission for the two polarization schemes (b). Principle of a two-color experiment (c) and corresponding experimental induced transmission for the two polarization schemes (d). Figure taken from Ref. [78].

The theoretical prediction of pronouncedly different roles of Coulomb scattering versus carrier phonon scattering in the process of reaching a thermalized isotropic carrier distribution calls for an experiment of similar distinctiveness. In that experiment, we make use of the strongly quenched optical phonon emission for $E < \hbar\Omega$ demonstrated in section 2. As depicted in **Figure 6b**, the anisotropy is preserved on a ps timescale when the photon energy is reduced to 88 meV [78]. This clearly shows that the quenching of optical phonon emission allows one to access a regime where the preferentially collinear Coulomb scattering preserves the anisotropic distribution over times that are much longer than the previously discussed 150 fs. Another conclusive test is provided by a two-color experiment (cf. Figure 6c and 6d). Here we increase the pump photon energy to 1.55 eV, while keeping the probe photon energy fixed at 88 meV. In this case, no anisotropic distribution is observed, pointing towards a rapid angular redistribution of excited carriers by optical phonons.

Let us stress that the comparison of the degenerate and two-color experiments actually provides insights that go beyond of what we have discussed in section 2. Since pump and probe photon energies were varied simultaneously in the degenerate pump-probe experiments presented in section 2, one cannot distinguish which effects are related to pump and probe photon energy, respectively. Many studies strongly suggest that it is the *probe* beam energy which crucially determines the observed dynamics. Firstly, the similar relaxation times of 10 – 20 ps obtained in our low-energy degenerate pump-probe experiments and in optical-pump THz-probe experiments support this hypothesis [52,79]. Secondly, there is clear evidence for the formation of a hot-carrier distribution on a sub-100 fs timescale [16,21,39,44,45]. Consequently, the value of the pump-photon energy should not matter at times beyond ~ 100 fs. In fact, this assumption is the basis of the thermodynamic model developed by D. Turchinovich's group [44]. This model has described the results of a variety

of experiments very successfully [44,46,80]. However, our findings depicted in Figure 6 indicate that the electronic system in graphene can “remember” the pump energy even on a ps timescale. Apparently, in the regime of low photon energies and low fluences the thermodynamics model can fail to predict all aspects of the carrier dynamics. In this regime, both non-collinear Coulomb scattering and carrier-phonon scattering are sufficiently slow to preserve an anisotropic – and consequently not fully thermalized – carrier distribution on a ps timescale.

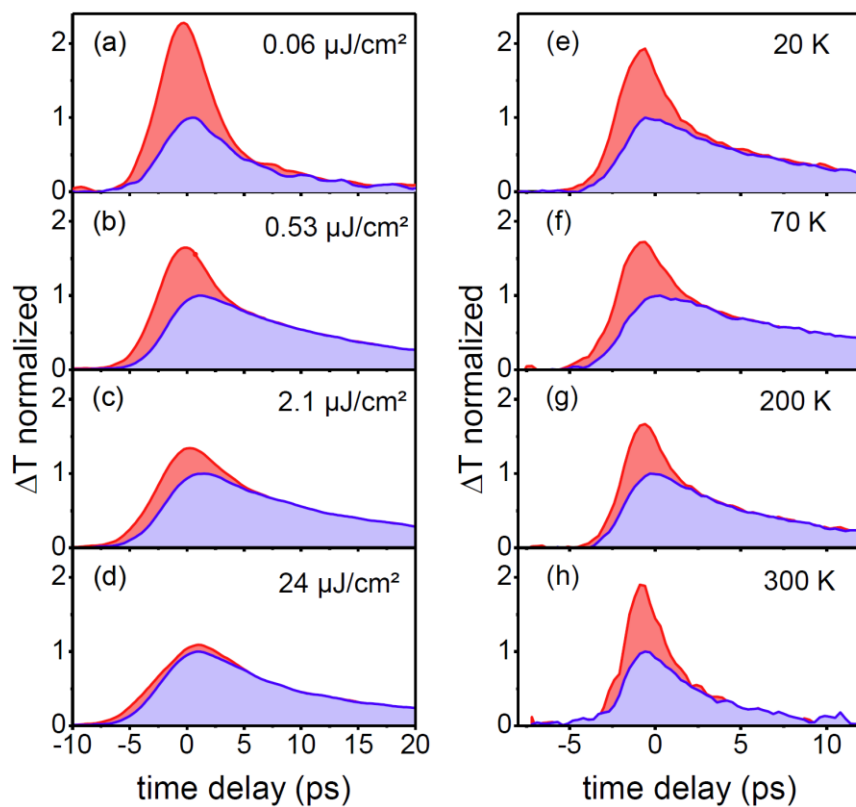


Figure 7: Experimental pump-induced transmission in degenerate pump-probe experiments at a photon energy of 88 meV. The red transients correspond to parallel, the blue to perpendicular orientation of the probe polarization with respect to the pump polarization. In the left column (a-d) the pump fluence is varied, while the substrate temperature is kept

constant at 20 K. In the right column (e-h) the pump fluence is kept constant at $1\mu\text{J}/\text{cm}^2$ while the substrate temperature is varied. Figure adapted from Ref. [78].

Finally, we make use of the quenched optical phonon emission to trace the non-collinear Coulomb scattering. In **Figure 7** the results of degenerate pump-probe experiments at $E = 88$ meV are presented. The difference between the two transmission transients obtained in the two polarization configurations becomes smaller with increasing fluence. This is a consequence of the increased number of photoexcited electrons in the conduction band at higher fluences. Naturally, the higher number of electrons results in a higher probability for non-collinear Coulomb scattering. Varying the substrate temperature, on the other hand, essentially does not affect the observed anisotropy of the carrier distribution. The only change induced by temperature variation is the cooling time: it becomes shorter for the highest substrate temperature of 300 K, which can be related to increased carrier-phonon scattering [40,78]. However, the cooling time is still longer than the timescale of non-collinear Coulomb scattering. Thus, the temperature increase from 200 K to 300 K does not diminish the observed anisotropy, which indicates that the decay time of the anisotropy is comparable to the duration of the excitation pulse (4 ps) even at room temperature. Not shown here, but discussed in Ref. [78], microscopic theory reveals the same trends as seen in the experiment.

With regard to potential applications the fairly long-lived anisotropic carrier distribution may be attractive. Many optoelectronic devices such as detectors [81,82,83], optically switched THz modulators [84], or saturable absorbers [85] rely on hot carriers. One may exploit the anisotropic distribution induced by linearly polarized radiation in devices with optimized electrode geometry. It is particularly attractive for applications that the anisotropic distribution is maintained over several picoseconds and not just femtoseconds, even at room temperature.

Our study was focused on almost intrinsic graphene. It remains an interesting question for further investigations in what manner electrons in the conduction band (or, equivalently, holes in the valence band), provided by doping, influence the Coulomb scattering dynamics of photoexcited carriers.

In the following section we use the gained knowledge of the carrier dynamics in a wide spectral range for an application example, namely an ultra-broadband high-speed detector based on a bolometric effect by hot electrons.

4. Fast ultra-broadband graphene based detectors

The conversion of optical into electrical signals by fast detectors with a temporal resolution of less than 100 ps is important for optical communication applications as well as for fundamental research. Depending on the spectral region, these detectors are based on different operation principles. In the ultraviolet (UV), VIS, and NIR spectral range, photoconductive detectors based on interband excitations in semiconductors are widely used [86]. Using narrow-gap semiconductors such as mercury cadmium telluride (MCT), this mechanism can also be employed in fast MIR detectors [87]. However, in the far-infrared (FIR) and THz frequency range different principles are required. Hot-electron bolometers (HEBs) that exploit the superconducting-to-normal phase transition feature fast response, large spectral bandwidth, and high sensitivity [88]. However, they have to be operated at cryogenic temperatures. Fast room temperature detectors in the THz region can be based on the photon drag effect [89] or on rectification, e.g. realized in Schottky diodes [90], field-effect transistors (FETs) [91], or superlattice detectors [92]. The sensitivity of rectifiers rolls off rapidly towards higher frequency. This limits their operation typically to the lower THz range, even though some devices function at frequencies above 20 THz [93]. Broadband THz operation is achieved by either coupling the detector element to a broadband antenna or by a large area detector design. A large number of graphene-based detectors exploiting various mechanisms such as the photoconductive effect [94], photo-thermoelectric effect [95,96], bolometric effect [97] and rectification in field-effect transistors [98] have been demonstrated. Different devices cover different spectral regions from the THz to the UV range (for a review see Ref. [12]). Here we present a fast room temperature operated detector where one single detector element covers the spectral range from THz to VIS.

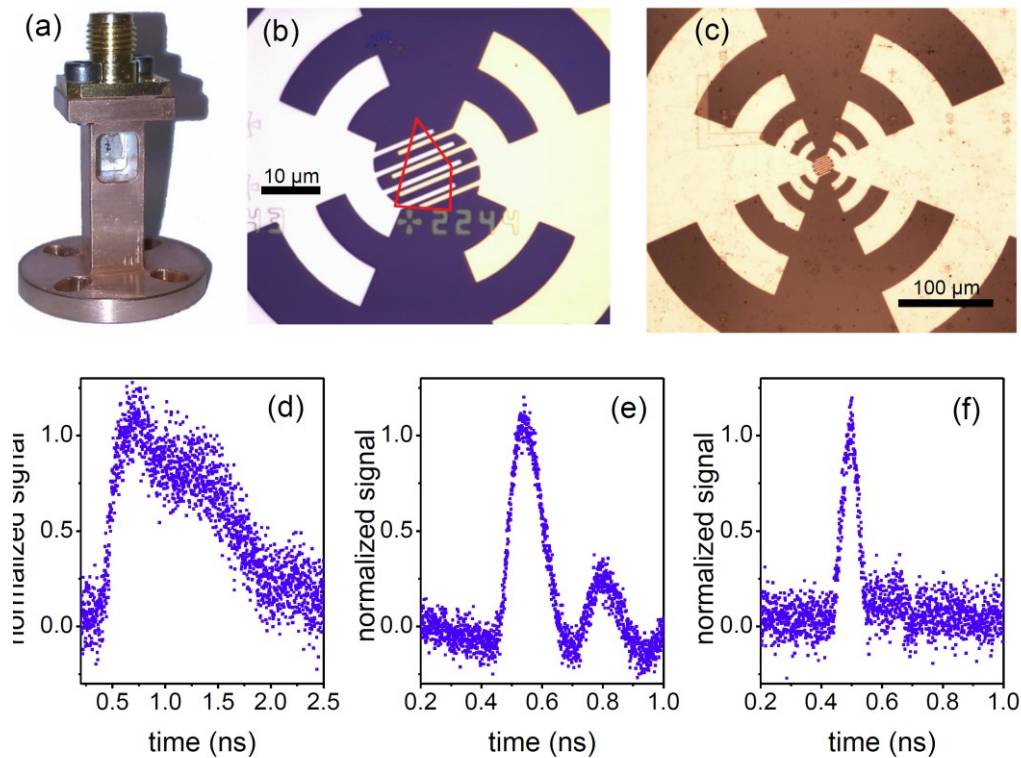


Figure 8: Detector in a copper block with SMA connector (a). Optical micrograph of the inner part of the antenna of a detector element of the second generation with the outline of the graphene flake marked in red (b). Optical micrograph of a detector of the third generation (c). Signal transients from detector elements of the first (d), second (e), and third generation (f), exposed to radiation pulses of 4.4 THz (d and e) and 28 THz, respectively. Part (b), (d) and (e) are adapted from Ref. [99], part (a), (c) and (f) from Ref. [83]. The differences between the three generations of detectors are explained in the main text.

All our detectors consist of a doped single-layer graphene flake (size 10 – 30 μm range) contacted to a logarithmic periodic antenna via interdigitated electrodes (**Figure 8b and 8c**). The antenna allows one to efficiently collect radiation of wavelength larger than the graphene flake. The outer part of the antenna is contacted to an SMA connector via a strip line. We have fabricated detectors in three different configurations. The first generation was based on

an exfoliated graphene flake on doped Si covered by SiO₂. Here, two types of metals (Au/Ti and Pt) were used for the two arms of the antenna (Figure 8b). Second generation detectors again employ exfoliated graphene, but on intrinsic Si/SiO₂ substrates and with Au/Ti layers for both antenna arms. For the third generation, graphene grown by chemical vapor deposition (CVD) transferred to a SiC substrate is applied in conjunction with Au/Ti metallized antenna arms (Figure 8c). We find that the photo-thermoelectric effect due to different Seebeck coefficients and the bolometric effect contribute almost equally to the obtained signal in the detectors with two different metallizations. At zero bias, only the photo-thermoelectric response is observed. The other detectors require a bias voltage for symmetry breaking and rely solely on the bolometric mechanism, which is explained in detail at the end of this section.

Due to the large capacitance provided by the doped silicon and the antenna, detectors of the first generation feature fairly long fall times (ns range) of the signals (Figure 8d). In contrast, the detectors on insulating substrates are very fast. For the third generation, SiC is chosen as a substrate in order to increase the spectral bandwidth. The absorption by interband transitions as well as phononic absorption in the substrate limit the spectral bandwidth of the second generation to frequencies below 10 THz [99]. The use of SiC with a bandgap of 3 eV as a substrate for the third generation of detectors enables operation from THz to VIS without any gap. This has been demonstrated by using various pulsed laser sources (THz gas laser, free-electron laser, frequency doubled fiber laser) from 0.6 THz ($\lambda = 496 \mu\text{m}$, $E = 2.5 \text{ meV}$) to 384 THz ($\lambda = 780 \mu\text{m}$, $E = 1.6 \text{ eV}$) [83]. Notably, no degraded performance is observed in the region of strong phononic absorption in SiC (24 THz – 50 THz), cf. Figure 8f. To the best of our knowledge such an ultra-broadband operation has not been shown previously for any fast detector. We expect the upper frequency limit of the detector to be 725 THz ($\lambda = 413 \text{ nm}$), corresponding to the 3 eV band gap of SiC. On the low frequency side we do not

expect a sharp cutoff. Basically the outer dimension of the antenna determines the longest wavelengths, which are still collected efficiently. The fast ultra-broadband detectors are very valuable for multicolor spectroscopy, where the timing of different pulsed sources has to be monitored and controlled [100].

In addition to the change in substrate, also the electric transmission line was improved for the third generation of detectors. This results in faster rise and fall times. Furthermore, better impedance matching almost eliminates the subsequent electrical pulses (see Figure 2e) caused by reflections of the electric signal. Detectors of the third generation are characterized by a rise time of 40 ps and a signal duration (full width at half maximum) of 45 ps [83].

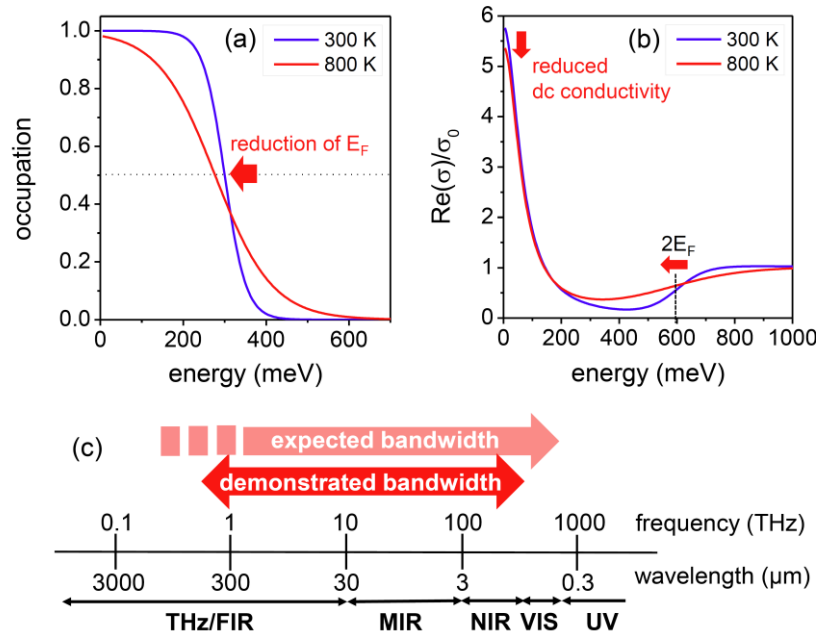


Figure 9: Calculated occupation in the conduction band of graphene featuring $E_f = 300$ meV (a). Real part of the dynamic conductivity in units of $\sigma_0 = e^2/4\hbar$, calculated for $E_f = 300$ meV and a momentum relaxation time of 10 fs (b). Schematic illustration of the spectral bandwidth of the detectors on SiC substrates (c).

As mentioned above, the detectors with similar metallization layers for both antenna arms require a bias voltage. Upon irradiation, the bias current through the graphene flake is

reduced. This behavior allows one to rule out a number of possible detection mechanisms, namely the photo-thermoelectric, photoconductive, photovoltaic, photogalvanic, and photon drag effects. The response can be explained, also quantitatively, by the bolometric effect [83]. The principle is illustrated in **Figure 9**. Heating of the carrier distribution results in a broadening of the Fermi edge. Furthermore, because of the linear increase of the density of states with energy, the chemical potential decreases with increasing temperature as the number of electrons remains constant (Figure 9a) [44]. This in turn modifies the dynamic conductivity. Since the spectral weight of the *interband* absorption is increased by the reduced Fermi energy, the spectral weight of the *intradband* Drude part has to decrease in order to fulfill the sum rule. The resulting reduced dc conductivity is responsible for the detector signal. In detail the response may be more complicated since the momentum relaxation time can also depend on electron temperature [44,101,102]. Nevertheless, the simple model considering just a temperature dependent chemical potential already provides an intuitive understanding of the mechanism and also allows us to quantitatively describe the detector response [83]. Consequently, the ultrabroadband detector presented here is a graphene-based HEB.

Figure 9b illustrates that the real part of the dynamic conductivity in typical CVD grown graphene at room temperature exhibits non-zero values for all photon energy, since the Drude peak at low energies merges with the broadened Fermi edge of the interband conductivity. As a result, the detector absorbs electromagnetic radiation at all energies. Note that a short momentum relaxation time, typically associated with low quality graphene, is actually helpful in this context as it yields a broad Drude peak.

Finally we attempt to discuss our HEB detector and other graphene-based detectors within general frame of fast detectors operated at room temperature. By fast, we consider here detectors with response times below 1 ns. The noise-equivalent power (NEP), even though

more difficult to specify, is a more valuable number as compared to the detector responsivity. Consequently, in **Figure 10** the NEP of a number of detectors is depicted over a wide frequency range from sub-THz to the visible spectral range. The NEP defines the minimum detectable power, thus a low NEP value stands for a sensitive detector. The NEP values presented here are related to the incident power on the detector. In some cases, in particular for the graphene-based HEB [99] and the GaAs FET detector [93], the noise of the electronic system exceeds the noise from the detector. Hence, the provided values should be considered as upper limits. We note that the graphene HEB, GaAs/AlGaAs superlattice detector [92] and the GaAs FET detector have been tested in a similar manner at FELBE. For the other detectors literature values are presented.

Photodiodes, e.g. based on GaAs, feature a very low NEP in the NIR range [103]. At the other side of the considered spectral range, namely at sub-THz frequencies, the same is true for Schottky diodes [104,105]. However, Schottky diodes are not well-suited for detection of short laser pulses due to their very low damage threshold. The NEP of Schottky diodes, the superlattice detector and the GaAs FET increases roughly quadratically with increasing frequency. This is the typical behavior of a rectifying detector due to the limitations imposed by RC time constants. FIR photon drag detectors [106, 107] exhibits a similar dependence, however the underlying physical origin is different. The NEP of the photon-drag detector increases quadratically with frequency because the free-carrier absorption in the doped semiconductor decreases quadratically. The strongly increasing NEP of many THz detectors towards higher frequencies causes a lack of fast sensitive detectors in the MIR region. This seems surprising, since in region MCT detectors show excellent performance. However, they require cooling and typically only reach response times in the range of 100 ns. There is a report on a MCT detector featuring a response time of about 1 ns, however no NEP is specified for that detector [108].

Our graphene HEB features a fairly high NEP, but it covers an extremely wide spectral range. In particular, it covers the MIR range, where not many fast, sensitive and room-temperature operated detectors exist. The other graphene-based detectors incorporated in the Figure 10 are a graphene-based FET [98] and a graphene photo-thermoelectric detector [109]. Detection with a fast response time has not been demonstrated for the FET, however, the detector design should enable fast operation. For the photo-thermoelectric detector a rather low NEP has been achieved. This detector has been applied to THz pulses and it should be possible to extend its spectral range. Similar to the improvement of the graphene HEB this may require replacing silicon by a better suited substrate material. Finally, it is worth noting that other novel two-dimensional materials also enter the scene as detector materials, as indicated by the photoconductive detector based on black phosphorous [110] and a photo-thermoelectric detector based on the same material [111].

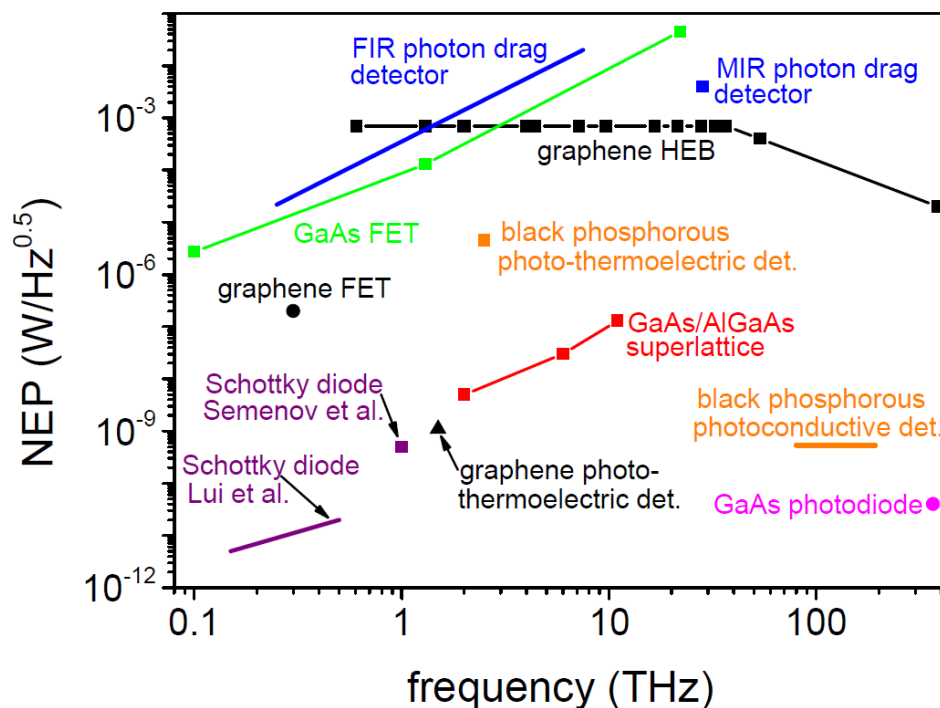


Figure 10: NEP of various fast and room-temperature operated detectors in the frequency range from sub-THz to NIR. The data for the graphene HEB and the GaAlAs superlattice

detector, an optimized version of the detector described in Refs. [92, 112] were measured at FELBE, as well as the data for the GaAs FET detector [93]. The data for the other detectors stem from the following sources: GaAs photodiode, Ref. [103]; black phosphorous based detectors photoconductive detector Ref. [110], and photo-thermoelectric detector Ref. [111]; graphene photo-thermoelectric detector, Ref. [109]; graphene-based FET, Ref. [98]; photon drag detectors for FIR and MIR, Refs. [89, 106, 107, 113]; Schottky diodes, Ref. [104,105].

5. Summary

We have shown that time resolved spectroscopy at low energies, i.e. in the range of the optical phonon energy and the Fermi energy, is very rewarding. Strong signatures in the experimental results, such as sign changes of the signals, provide direct evidence for microscopic processes such as interband versus intraband absorption. Moreover, the role of carrier-carrier and carrier phonon scattering can be disentangled clearly in experiments that make use of the optically induced anisotropy in graphene. The strong link between microscopic theory and experiments allows one to understand the underlying physical mechanisms in great detail. Our results may be attractive for optoelectronic device applications based on hot carriers such as detectors, modulators or saturable absorbers. As an example, we have demonstrated a graphene-based high-speed hot-electron bolometer operating at room temperature. Here a single detector element covers the spectral range from the THz to the visible region without any gap.

Acknowledgements

We thank P. Michel, W. Seidel, M. J. Klopff and the ELBE team for their dedicated support using FELBE and A. Pashkin for friendly collaboration. We are grateful for the growth of the epitaxial graphene samples by C. Berger and W. A. de Heer from the Georgia Institute of Technology. With respect to detector fabrication and testing, we thankfully acknowledge

significant contributions from J. Kerbusch and A. Erbe from HZDR as well as J. Kamann, S. D. Ganichev, J. Eroms and D. Weiss from the University of Regensburg. Furthermore, we are grateful for the Priority Program (SPP) 1459 Graphene organized by the German Research Foundation (DFG) and coordinated by Th. Seyller from Chemnitz University of Technology. For our project the collaboration within SPP 1459 with the two groups from Regensburg was very valuable, but also many fruitful discussions with other participants, in particular with F. Speck from Chemnitz University of Technology, D. Neumaier from AMO GmbH, and J. Maultzsch from TU Berlin.

Received: ((will be filled in by the editorial staff))

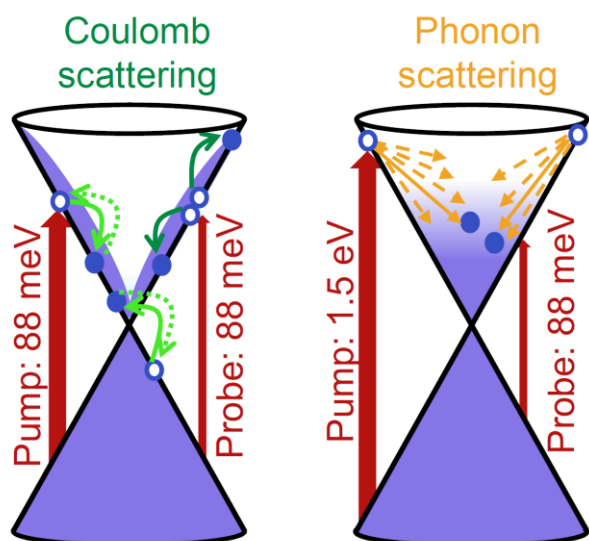
Revised: ((will be filled in by the editorial staff))

Published online: ((will be filled in by the editorial staff))

Keywords: graphene, carrier dynamics, ultrafast spectroscopy, broadband detection

Graphical Abstract

The carrier dynamics in graphene is investigated in a joint experiment-theory study, with a particular focus on optical excitations at low energies. The role of carrier-phonon and carrier-carrier scattering is clearly disentangled and a twofold behavior for carrier-carrier scattering is revealed: (i) fast collinear scattering and (ii) comparably slow non-collinear scattering. Furthermore fast ultrabroadband detectors, covering the range from THz to visible, are demonstrated.



ToC figure (quadratic format, no caption)

References

- [1] K. S. Novoselov, A. K. Geim, S. V. Morozov, D. Jiang, Y. Zhang, S. V. Dubonos, I. V. Grigorieva, and A. A. Firsov, *Science* **306**, 666-669 (2004).
- [2] A. K. Geim, and K. S. Novoselov, *Nat. Mat.* **6**, 183-191 (2007).
- [3] P. R. Wallace, *Phys. Rev.* **71**, 622-634 (1947).
- [4] K. S. Novoselov, A. K. Geim, and S. V. Morozov, *Nature* **438**, 197-200 (2005).
- [5] M. I. Katsnelson, K. S. Novoselov, and A. K. Geim, *Nat. Phys.* **2**, 620-625 (2006).
- [6] N. Stander, B. Huard, and D. Goldhaber-Gordon, *Phys. Rev. Lett.* **102**, 026807 (2009).
- [7] R. R. Nair, P. Blake, A. N. Grigorenko, K. S. Novoselov, T. J. Booth, T. Stauber, N. M. R. Peres, and A. K. Geim, *Science* **320**, 1308 (2008).
- [8] K. F. Mak, L. Ju, F. Wang, and T. F. Heinz, *Solid State Commun.* **152**, 1341-1349 (2012).
- [9] K. S. Novoselov, V. I. Fal'ko, L. Colombo, P. R. Gellert, M. G. Schwab, and K. Kim, *Nature* **490**, 192-200 (2012).
- [10] F. Bonaccorso, Z. Sun, T. Hasan, and A. C. Ferrari, *Nat. Photon.* **4**, 611-622 (2010).
- [11] A. C. Ferrari, F. Bonaccorso, V. Fal'ko, K. S. Novoselov, S. Roche, P. Boggild, S. Borini, F. H. L. Koppens, V. Palermo, N. Pugno, J. A. Garrido, R. Sordan, A. Bianco, L. Ballerini, M. Prato, E. Lidorikis, J. Kivioja, C. Marinelli, T. Ryhanen, A. Morpurgo, J. N. Coleman, V. Nicolosi, L. Colombo, A. Fert, M. Garcia-Hernandez, A. Bachtold, G. F. Schneider, F. Guinea, C. Dekker, M. Barbone, Z. Sun, C. Galiotis, A. N. Grigorenko, G. Konstantatos, A. Kis, M. Katsnelson, L. Vandersypen, A. Loiseau, V. Morandi, D. Neumaier, E. Treossi, V. Pellegrini, M. Polini, A. Tredicucci, G. M. Williams, B. Hee Hong, J.-H. Ahn, J. Min Kim, H. Zirath, B. J. van Wees, H. van der Zant, L. Occhipinti, A. Di Matteo, I. A. Kinloch, T. Seyller, E. Quesnel, X. Feng, K. Teo, N. Rupesinghe, P.

-
- Hakonen, S. R. T. Neil, Q. Tannock, T. Lofwander, and J. Kinaret, *Nanoscale* **7**, 4598 (2015).
- [12] F. H. L. Koppens, T. Mueller, Ph. Avouris, A. C. Ferrari, M. S. Vitiello and M. Polini, *Nat. Nanotechnol.* **9**, 780-793 (2014).
- [13] J. M. Dawlaty et al., *Appl. Phys. Lett.* **92**, 042116 (2008).
- [14] H. Wang, J. H. Strait, P. A. George, S. Shivaraman, V. B. Shields., M. Chandrashekhar, J. Hwang, F. Rana, M. G. Spencer, C. S. Ruiz-Vargas, and J. Park, *Appl. Phys. Lett.* **96**, 081917 (2010).
- [15] M. Breusing, C. Ropers, and T. Elsaesser, *Phys. Rev. Lett.* **102**, 086809 (2009).
- [16] M. Breusing, S. Kuehn, T. Winzer, E. Malić, F. Milde, N. Severin, J. P. Rabe, C. Ropers, A. Knorr, and T. Elsaesser, *Phys. Rev. B* **83**, 153410 (2011).
- [17] D. Sun, Z.-K. Wu, C. Divin, X. Li, C. Berger, W. A. de Heer, P. N. First, and T. B. Norris, *Phys. Rev. Lett.* **101**, 157402 (2008).
- [18] R.W. Newson, J. Dean, B. Schmidt, and H. M. van Drie, *Opt. Express* **17**, 2326 (2009).
- [19] D. Sun, C. Divin, C. Berger, W. A. de Heer, P. N. First, and T. B. Norris, *Phys. Rev. Lett.* **104**, 136802 (2010).
- [20] H. Choi, F. Borondics, D. A. Siegel, S. Y. Zhou, M. C. Martin, A. Lanzara, and R. A. Kaindl, *Appl. Phys. Lett.* **94**, 172102 (2009).
- [21] P. A. Obraztsov, M. G. Rybin, A. V. Tyurnina, S. V. Garnov, E. D. Obraztsova, A. N. Obraztsov, and Y. P. Svirkov, *Nano Lett.* **11**, 1540 (2011).
- [22] J. C. Johannsen, S. Ulstrup, F. Cilento, A. Crepaldi, M. Zacchigna, C. Cacho, I. C. E. Turcu, E. Springate, F. Fromm, C. Roidel, T. Seyller, F. Parmigiani, M. Grioni, and P. Hofmann, *Phys. Rev. Lett.* **111**, 027403 (2013).
- [23] I. Gierz, J. C. Petersen, M. Mitrano, C. Cacho, I. C. E. Turcu, E. Springate, A. Stöhr, A. Köhler, U. Starke, and A. Cavalleri, *Nat. Mater.* **12**, 1119 (2013).

-
- [24] S. Ulstrup, J. C. Johannsen, A. Crepaldi, F. Cilento, M. Zacchigna, C. Cacho, R. T. Chapman, E. Springate, F. Fromm, C. Raidel, T. Seyller, F. Parmigiani, M. Grioni, and Philip Hofmann, *J. Phys.: Condens. Matter* **27**, 164206 (2015).
- [25] T. Li, L. Luo, M. Hupalo, J. Zhang, M. C. Tringides, J. Schmalian, and J. Wang, *Phys. Rev. Lett.* **108**, 167401 (2012).
- [26] T. Winzer, E. Malic, and A. Knorr, *Phys. Rev. B* **87**, 165413 (2013).
- [27] R. Jago, T. Winzer, A. Knorr, and E. Malic, *Phys. Rev. B* **92**, 085407 (2015).
- [28] T. Winzer, A. Knorr, and E. Malic, *Nano Lett.* **10**, 4839-4843 (2010).
- [29] S. Tani, F. Blanchard, and K. Tanaka, *Phys. Rev. Lett.* **109**, 166603 (2012).
- [30] K. J. Tielrooij, J. C. W. Song, S. A. Jensen, A. Centeno, A. Pesquera, A. Z. Elorza, M. Bonn, L. S. Levitov, and F. H. L. Koppens, *Nat. Phys.* **9**, 248 (2013).
- [31] D. Brida, W. A. Tomadin, C. Manzoni, Y.J. Kim, A. Lombardo, S. Milana, R. R. Nair, K. S. Novoselov, A. C. Ferrari, G. Cerullo and M. Polini, *Nat. Commun.* **4**, 1987 (2013).
- [32] T. Plötzing, T. Winzer, E. Malic, D. Neumaier, A. Knorr, and H. Kurz, *Nano Lett.* **14**, 5371 (2014).
- [33] T. Winzer and E. Malic, *Phys. Rev. B* **85**, 241404(R) (2012).
- [34] F. Kadi, T. Winzer, A. Knorr, and E. Malic, *Sci. Rep.* **5**, 16841 (2015).
- [35] F. Wendler, A. Knorr, and E. Malic, *Nat. Commun.* **5**, 3703 (2014).
- [36] E. Malic, T. Winzer, F. Wendler, and A. Knorr, *Phys. Status Solidi B* **253**, 2303 (2016).
- [37] C. Berger, Z. Song, X. Li, X. Wu, N. Brown, C. Naud, D. Mayou, T. Li, J. Hass, A. N. Marchenkov, E. H. Conrad, P. N. First, and W. A. de Heer, *Science* **312**, 1191 (2006).
- [38] M. Sprinkle, D. Siegel, Y. Hu, J. Hicks, A. Tejada, A. Taleb-Ibrahimi, P. Le Fèvre, F. Bertran, S. Vizzini, H. Enriquez, S. Chiang, P. Soukiassian, C. Berger, W. A. de Heer, A. Lanzara, and E. H. Conrad, *Phys. Rev. Lett.* **103**, 226803 (2009).

-
- [39] S. Winnerl, F. Göttfert, M. Mittendorff, H. Schneider, M. Helm, T. Winzer, E. Malic, A. Knorr, M. Orlita, M. Potemski, M. Sprinkle, C. Berger, and W. A. de Heer, *J. Phys.: Condens. Matter* **25**, 054202 (2013).
- [40] S. Winnerl, M. Orlita, P. Plochocka, P. Kossacki, M. Potemski, T. Winzer, E. Malic, A. Knorr, M. Sprinkle, C. Berger, W. A. de Heer, H. Schneider, and M. Helm, *Phys. Rev. Lett.* **107**, 237401 (2011).
- [41] E. Malic and A. Knorr, *Graphene and Carbon Nanotubes: Ultrafast Optics and Relaxation Dynamics*, 1st ed. (Wiley-VCH, 2013).
- [42] E. Malic, T. Winzer, E. Bobkin, and A. Knorr, *Phys. Rev. B* **84**, 205406 (2011).
- [43] T. Winzer and E. Malic, *J. Phys.: Condens. Matter* **25**, 054201 (2013).
- [44] Z. Mics, K.-J. Tielrooij, K. Parvez, S. A. Jensen, I. Ivanov, X. Feng, K. Müllen, M. Bonn, and D. Turchinovich, *Nat. Commun.* **6**, 7655 (2015).
- [45] I. Gierz, F. Calegari, S. Aeschlimann, M. Chávez Cervantes, C. Cacho, R. T. Chapman, E. Springate, S. Link, U. Starke, C. R. Ast, and A. Cavalleri, *Phys. Rev. Lett.* **115**, 086803 (2015).
- [46] R. J. Suess, S. Winnerl, H. Schneider, M. Helm, C. Berger, W. A. de Heer, T. E. Murphy, and M. Mittendorff, *ACS Photonics* **3**, 1069–1075 (2016).
- [47] F. Kadi, T. Winzer, E. Malic, A. Knorr, F. Göttfert, M. Mittendorff, S. Winnerl, and M. Helm, *Phys. Rev. Lett.* **113**, 035502 (2014).
- [48] P. Plochocka, P. Kossacki, A. Golnik, T. Kazimierczuk, C. Berger, W. A. de Heer, and M. Potemski, *Phys. Rev. B* **80**, 245415 (2009).
- [49] J. Shang, Z. Luo, C. Cong, J. Lin, T. Yu, and G. G. Gurzadyan, *Appl. Phys. Lett.* **97**, 163103 (2010).
- [50] L. M. Malard, K. F. Mak, A. H. C. Neto, N.M. R. Peres, and T. F. Heinz, *New J. Phys.* **15**, 015009 (2013).

-
- [51] S. Massabeau, M. Baillergeau, T. Phuphachong, C. Berger, W. A. de Heer, S. Dhillon, J. Tignon, L. A. de Vaultier, R. Ferreira, and J. Mangeney, *Phys. Rev. B* **95**, 085311 (2017)
- [52] P. A. George, J. Strait, J. Dawlaty, S. Shivaraman, M. Chandrashekar, F. Rana and M. G. Spencer, *Nano Lett.* **8**, 4248-4251 (2008).
- [53] J. H. Strait, H. Wang, S. Shivaraman, V. Shields, M. Spencer, and F. Rana, *Nano Lett.* **11**, 4902-4906 (2011).
- [54] R. Kießling, “Terahertz-Dynamik optisch angeregter Ladungsträger in Graphen”, Masterarbeit an der TU Ilmenau (2015).
- [55] S. F. Shi, T.-T. Tang, B. Zeng, L. Ju, Q. Zhou, A. Zettl, and F. Wang, *Nano Lett.* **14**, 1578-1582 (2014).
- [56] A. J. Frenzel, C. H. Lui, Y. C. Shin, J. Kong, and N. Gedik, *Phys. Rev. Lett.* **113**, 056602 (2014).
- [57] H. Y. Hwang, N. C. Brandt, H. Farhat, A. L. Hsu, J. Kong, and K. A. Nelson, *J. Phys. Chem. B* **117**, 15819-15824 (2013).
- [58] G. Jnawali, Y. Rao, H. Yan, and T. F. Heinz, *Nano Lett.* **13**, 524-530 (2013).
- [59] E. J. Mele, P. Král, and D. Tománek, *Phys. Rev. B* **61**, 7669 (2010).
- [60] A. Grüneis, R. Saito, G. G. Samsonidze, T. Kimura, M. A. Pimenta, A. Jorio, A. G. Souza Filho, G. Dresselhaus, and M. S. Dresselhaus, *Phys. Rev. B* **67**, 165402 (2003).
- [61] A. P. Heberle, W. W. Rühle, and K. Ploog, *Phys. Rev. Lett.* **72**, 3887-3890 (1994).
- [62] C. Fürst, A. Leitenstorfer, A. Laubereau, and R. Zimmermann, *Phys. Rev. Lett.* **78**, 3733-3736 (1997).
- [63] T. C. Damen, L. Viña, J. E. Cunningham, and J. Shah, *Phys. Rev. Lett.* **67**, 3432-3435 (1991).

-
- [64] J. Wagner, H. Schneider, D. Richards, A. Fischer, and K. Ploog, *Phys. Rev. B* **47**, 4786-4789 (1991).
- [65] M. Trushin and J. Schliemann, *Europhys. Lett.* **96**, 37006 (2011).
- [66] T. J. Echtermeyer, P. S. Nene, M. Trushin, R. V. Gorbachev, A. L. Eiden, S. Milana, Z. Sun, J. Schliemann, E. Lidorikis, K. S. Novoselov, and A. C. Ferrari, *Nano Lett.* **14**, 3733 (2014).
- [67] C. Töke, P. E. Lammert, V. H. Crespi, and J. K. Jain, *Phys. Rev. B* **74**, 235417 (2006).
- [68] M. O. Goerbig, *Rev. Mod. Phys.* **83**, 1193-1243 (2011).
- [69] D. Sun, C. Divin, J. Rioux, J. E. Sipe, C. Berger, W. A. de Heer, P. N. First, and T. B. Norris, *Nano Lett.* **10**, 1293-1296 (2010).
- [70] D. Sun, C. Divin, M. Mihnev, T. Winzer, E. Malic, A. Knorr, J. E. Sipe, C. Berger, W. A. de Heer, P. N. First, and T. B. Norris, *New J. Phys.* **14**, 105012 (2012).
- [71] M. Kim, H. A. Yoon, S. Woo, D. Yoon, S. W. Lee, and H. Cheong, *Appl. Phys. Lett.* **101**, 073103 (2012).
- [72] M. Mittendorff, T. Winzer, E. Malic, A. Knorr, C. Berger, W. A. de Heer, H. Schneider, M. Helm, and S. Winnerl, *Nano Lett.* **14**, 1504 (2014).
- [73] M. Trushin, A. Grupp, G. Soavi, A. Budweg, D. De Fazio, U. Sassi, A. Lombardo, A. C. Ferrari, W. Belzig, A. Leitenstorfer, and D. Brida, *Phys. Rev. B* **92**, 165429 (2015).
- [74] X.-Q. Yan, J. Yao, Z.-B. Liu, X. Zhao, X.-D. Chen, C. Gao, W. Xin, Y. Chen, and J.-G. Tian, *Phys. Rev. B* **90**, 134308 (2014).
- [75] X.-Q. Yan, F. Liu, X.-T. Kong, J. Yoa, X. Zhao, Z.-B. Liu, and J.-G. Tian, *J. Opt. Soc. Am. B* **36**, 218-226 (2017).
- [76] E. Malic, T. Winzer, and A. Knorr, *Appl. Phys. Lett.* **101**, 213110 (2012).
- [77] F. Rana, P. A. George, J. H. Strait, J. Dawlaty, S. Shivaraman, M. Chandrashekar, and M. G. Spencer, *Phys. Rev. B* **79**, 115447 (2009).

-
- [78] J. C. König-Otto, M. Mittendorff, T. Winzer, F. Kadi, E. Malic, A. Knorr, C. Berger, W. A. de Heer, A. Pashkin, H. Schneider, M. Helm, and S. Winnerl, *Phys. Rev. Lett.* **117**, 087401 (2016).
- [79] M. T. Mihnev, F. Kadi, C. J. Divin, T. Winzer, S. Lee, C.-H. Liu, Z. Zhong, C. Berger, W. A. de Heer, E. Malic, A. Knorr, and T. B. Norris, *Nat. Commun.* **7**, 11617 (2016).
- [80] S. A. Jensen, Z. Mics, I. Ivanov, H. S. Varol, D. Turchinovich, F. H. L. Koppens, M. Bonn, and K. J. Tielrooij, *Nano Lett.* **14**, 5839 (2014).
- [81] T. Mueller, F. Xia, and P. Avouris, *Nat. Photonics* **4**, 297 (2010).
- [82] V. Ryzhii, A. Satou, T. Otsuji, M. Ryzhii, V. Mitin, and M. S. Shur, *J. Appl. Phys.* **116**, 114504 (2014).
- [83] M. Mittendorff, J. Kamann, J. Eroms, D. Weiss, C. Drexler, S. D. Ganichev, J. Kerbusch, A. Erbe, R. J. Suess, T. E. Murphy, S. Chatterjee, K. Kolata, J. Ohser, J. C. König-Otto, H. Schneider, M. Helm, and S. Winnerl, *Opt. Express* **23**, 28728 (2015).
- [84] Q.-Y. Wen, W. Tian, Q. Mao, Z. Chen, W.-W. Liu, Q.-H. Yang, M. Sanderson and H.-W. Zhang, *Sci. Rep.* **4**, 7409 (2014).
- [85] D. G. Purdie, D. Popa, V. J. Wittwer, Z. Jiang, G. Bonacchini, F. Torrisi, S. Milana, E. Lidorikis, and A. C. Ferrari, *Appl. Phys. Lett.* **106**, 253101 (2015).
- [86] Y. G. Wey, D. L. Crawford, K. Giboney, J. E. Bowers, M. J. Rodwell, P. Silvestre, M. J. Hafich, and G. Y. Robinson, *Appl. Phys. Lett.* **58**, 2156 (1991).
- [87] M. Kopytko, K. Jozwikowski, A. Jozwikowska, and A. Rogalski, *Opto-Electron. Rev.* **18**, 277-283 (2010).
- [88] A. D. Semenov, G. N. Gol'tsman, and R. Sobolewski, *Supercond. Sci. Technol.* **15**, R1-R16 (2002).
- [89] S. D. Ganichev, Y. V. Terent'ev, and I. D. Yaroshetskii, *Sov. Tech. Phys. Lett.* **11**, 20 (1985).

-
- [90] A. Semenov, O. Cojocari, H.-W. Hübers, F. Song, A. Klushin, and A.-S. Müller, *IEEE Electron Device Lett.* **31**, 674-676 (2010).
- [91] F. Teppe, D. Veksler, V. Yu. Kachorovski, A. P. Dmitriev, X. Xie, X.-C. Zhang, S. Rumyantsev, W. Knap, and M. S. Shur, *Appl. Phys. Lett.* **87**, 022102 (2005).
- [92] F. Klappenberger, A. A. Ignatov, S. Winnerl, E. Schomburg, W. Wegscheider, K. F. Renk, and M. Bichler, *Appl. Phys. Lett.* **78**, 1673 (2001).
- [93] S. Regensburger, M. Mittendorff, S. Winnerl, H. Lu, A. C. Gossard, and S. Preu, *Opt Express* **23**, 20732-20742 (2015).
- [94] Y. Yao, R. Shankar, P. Rauter, Y. Song, J. Kong, M. Loncar, and F. Capasso, *Nano Lett.* **14**, 3749-3754 (2014).
- [95] X. Xu, N. M. Gabor, J. S. Alden, A. M. van der Zande, and P. L. McEuen, *Nano Lett.* **10**, 562-566 (2010).
- [96] X. Cai, A. B. Sushkov, R. J. Suess, M. M. Jadidi, G. S. Jenkins, L. O. Nyakiti, R. L. Myers-Ward, S. Li, J. Yan, D. K. Gaskill, T. E. Murphy, H. D. Drew, and M. S. Fuhrer, *Nat. Nanotechnol.* **9**, 814–819 (2014).
- [97] C. B. McKitterick, H. Vora, X. Du, B. S. Karasik, and D. E. Prober, *J. Low Temp. Phys.* **176**, 291-298 (2014).
- [98] L. Vicarelli, M. S. Vitiello, D. Coquillat, A. Lombardo, A. C. Ferrari, W. Knap, M. Polini, V. Pellegrini, and A. Tredicucci, *Nat. Mater.* **11**, 865-871 (2012).
- [99] M. Mittendorff, S. Winnerl, J. Kamann, J. Eroms, D. Weiss, H. Schneider, and M. Helm, *Appl. Phys. Lett.* **103**, 021113 (2013).
- [100] J. Bhattacharyya, M. Wagner, S. Zybell, S. Winnerl, D. Stehr, M. Helm, and H. Schneider, *Rev. Sci. Instrum.* **82**, 103107 (2011).
- [101] E. Hwang and S. Das Sarma, *Phys. Rev. B* **77**, 115449 (2008).

-
- [102] S. Das Sarma, S. Adam, E. H. Hwang, and E. Rossi, *Rev. Mod. Phys.* **83**, 407-470 (2011).
- [103] C. J. Wei, H.-J. Klein, and H. Benking, *Electron. Lett.* **17**, 688-690 (1981).
- [104] L. Liu, J. L. Hesler, H. Xu, Member, A. W. Lichtenberger, and R. M. Weikle, *IEEE Microwave and Wireless Components Lett.* **20**, 1531-1309 (2010).
- [105] A. Semenov, O. Cojocari, H.-W. Hübers, F. Song, A. Klushin, and A.-S. Müller, *IEEE Electron Device Lett.*, **31**, 674-676 (2010).
- [106] S. D. Ganichev and W. Prettl, *Intense terahertz excitation of semiconductors*, 1st ed. (Oxford University Press, 2006)
- [107] The datasheet of the FIR detector PD3F (Ioffe institute) can be found at <http://www.physik.uni-regensburg.de/forschung/ganichev/english/fields/advertisment/pdd99.pdf>
- [108] M. Kopytko, K. Jozwikowski, A. Jozwikowska, and A. Rogalski, *Opt.-Electron. Rev.* **18**, 277–283 (2010).
- [109] X. Cai, A. B. Sushkov, R. J. Suess, M. M. Jadidi, G. S. Jenkins, L. O. Nyakiti, R. L. Myers-Ward, S. Li, J. Yan, D. K. Gaskill, T. E. Murphy, H. D. Drew and M. S. Fuhrer, *Nat. Nanotechnol.* **9**, 814-819 (2014).
- [110] R. J. Suess, E. Leong, J. L. Garrett, T. Zhou, R. Salem, J. N. Munday, T. E. Murphy and M. Mittendorff, *2D Mater.* **3**, 041006 (2016).
- [111] E. Leong, R. J. Suess, A. B. Sushkov, H. D. Drew, T. E. Murphy, and M. Mittendorff, *Opt. Express* **25**, 12666-12674 (2017).
- [112] S. Winnerl, W. Seiwerth, E. Schomburg, J. Grenzer, K. F. Renk, C. J. G. M. Langerak, A. F. G. van der Meer, D. G. Pavel'ev, Yu. Koschurinov, A. A. Ignatov, B. Melzer, V. Ustinov, S. Ivanov, and P. S. Kop'ev, *Appl. Phys. Lett.* **73**, 2983 (1998).

[113] The datasheet of the detector B749 from Hamamatsu can be found at

<http://www.hamamatsu.com/us/en/product/alpha/I/4007/4147/B749/index.html>